AN INSTRUMENT TO OBSERVE LOW-DEGREE SOLAR OSCILLATIONS

S. TOMCZYK, K. STREANDER, G. CARD, D. ELMORE and H. HULL
High Altitude Observatory, NCAR, P.O. Box 3000, Boulder, CO 80307, U.S.A.*

and

A. CACCIANI
University of Rome 'La Sapienza', Rome, Italy

(Received 1 November, 1994; in revised form 24 February, 1995)

Abstract. We have constructed an instrument optimized to observe solar oscillations of low degree. The primary goal of this instrument, which we call LOWL, is to measure the frequency splitting of the low-degree modes in order to determine the rotation rate of the solar core. The LOWL is a Doppler imager based on a magneto-optical filter. It employs a two-beam technique to simultaneously observe solar images in opposite wings of the absorption line of potassium at 769.9 nm. This instrument is very stable against drifts in the wavelength zero-point, is insensitive to noise sources due to intensity fluctuations and image motion, and has a Doppler analyzer with no moving parts. The LOWL has been deployed at HAO's observing station on Mauna Loa, Hawaii and will operate for a period of at least two years.

1. Introduction

Over the past two decades, the p-mode oscillations have been successfully employed as a diagnostic of solar sub-surface structure and rotation. Standard solar models are now able to predict p-mode eigenfrequencies that are consistent with measurements to a level of about 0.1%, providing confidence in our understanding of the physics governing solar and stellar structure (Cox, Guzik, and Kidman, 1989; Guzik and Cox, 1991). In particular, measurements of p-mode eigenfrequencies constrain the depth of the solar convection zone (Rhodes, Ulrich, and Simon, 1977; Christensen-Dalsgaard, Gough, and Thompson, 1991), the solar envelope helium abundance (Guzik and Cox, 1992; Dziembowski, Pamyatnykh, and Sienkiewicz, 1991; Vorontsov, Baturin, and Pamyatnykh, 1991), and the solar rotation profile over the outer half of the Sun (Goode *et al.*, 1991, and references therein). The capabilities of helioseismology are discussed in greater detail in reviews of the subject (Brown, Mihalas, and Rhodes, 1986; Christensen-Dalsgaard, Gough, and Toomre, 1985; Harvey, 1988). Unfortunately, current observations of the frequency splitting of low-degree p-modes lack sufficient precision to constrain the solar rotation rate interior to 0.4 $R_\odot$. This measurement bears directly on several important questions including the distribution and evolution of solar and stellar angular momentum (Pinsonneault *et al.*, 1989; MacGregor and Brenner, 1991; Charbonneau and MacGregor, 1992), the solar dynamo (Gilman, Morrow, and DeLuca, 1989; Wilson,

* The National Center for Atmospheric Research is sponsored by the National Science Foundation.

1992), and the solar quadrupole moment with its implications to general relativity (Hill, Bos, and Goode, 1982).

To address these problems, we have constructed an instrument specifically optimized for the observation of solar oscillations of low degree (LOWL). The instrument combines an atomic vapor wavelength standard which provides an extremely stable velocity zero point, with a two-beam technique which simultaneously records the intensity over the solar disk in opposite wings of a solar absorption line with moderate spatial resolution. This combination produces an instrument with unprecedented capability to observe the low-degree oscillations.

This paper provides a detailed description of the LOWL instrument. In the following section we discuss the general instrument requirements which have led to the current design. A detailed description of the various components of the instrument are given in Section 3, and in Section 4 we present an evaluation of instrument performance. The preliminary results of our initial observations are presented in Section 5.

2. Instrument Requirements

The conceptual design of this instrument has been driven by several solar oscillation properties. The first property is that the p-mode lifetimes are short with respect to a solar rotation period. This means that mode linewidths are comparable to the rotational frequency splitting resulting in the overlapping of modes in a given multiplet in the power spectra from integrated light observations, except at extremely low frequencies (e.g., Loudagh *et al.*, 1993). Although several groups have reported the measurement of large frequency splittings with integrated light experiments (Claverie *et al.*, 1981; Toutain and Fröhlich, 1992; Loudagh *et al.*, 1993), a lack of consensus persists about solar core rotation. Observations with spatial resolution, however, allow the isolation of individual modes, as well as the separation of prograde and retrograde traveling waves. This gives spatially resolved observations a distinct advantage over integrated light observations for the purpose of measuring rotational frequency splittings with minimal systematic error.

Observations of the Sun from the Earth are limited to only one solar hemisphere. This loss of information prevents the observational isolation of signal from modes with nearby degree and azimuthal order. This effect is extremely important since any fluctuations in the zero-point of the instrument will be seen directly in the $l = 0$ time series, and will leak into the higher degree time series producing a type of spatial $1/f$ noise. Coupling of modes to the zero-point decreases with increasing degree; the coupling is near unity at $l = 1$, $\sim 0.1\%$ at $l = 5$, and decreases to negligible values at higher degree. The constraint which this places on the stability of a low-degree instrument can be estimated by integrating a model of the solar background velocity noise (Harvey, 1985) over the five-minute band, and implies a zero-point stability of < 0.5 m s^{-1} r.m.s. This stringent requirement accounts

for the general difficulty in observing low-degree oscillations, and is the reason that low-degree observations have been primarily limited to instruments which incorporate atomic wavelength standards.

For observations of long duration, the ability to measure mode frequencies is fundamentally limited by the property that the oscillations are stochastically driven and have a finite lifetime (Duvall and Harvey, 1986; Sorensen, 1988). Assuming the observations are limited by this so-called 'realization noise', it is estimated that one year of observations will result in an average $l = 1$ frequency splitting accurate to 10 nHz (Veitzer, Tomczyk, and Schou, 1992). Simulations of low-degree time series (Veitzer, Tomczyk, and Schou, 1992) indicate that observations from one site with a duty cycle of ~ 0.3 can approach the realization noise limit.

Observation of the oscillations in the solar velocity field allows higher signal-to-background measurements than intensity observations by a factor of ~ 50 in power (Duvall, Harvey, and Pomerantz, 1988). Significant sky transparency fluctuations also offer a serious impediment to ground-based intensity observations (e.g., Grec *et al.*, 1977). These fluctuations are a serious source of low-degree noise for instruments where a velocity signal is obtained by chopping between intensity signals.

To summarize, the low-degree oscillations can be optimally observed by an instrument with spatial resolution in the solar velocity field. The instrument must be extremely stable and, if ground based, it must minimize the effects of atmospherically-induced fluctuations. The instrument must be capable of operating over a time scale of years. These requirements are met by the LOWL instrument, which is described in the following section.

3. Instrument Description

The LOWL instrument is situated about 10 m south of the Mauna Loa Solar Observatory (MLSO) located at an elevation of 3414 m on Mauna Loa on the island of Hawaii. Figure 1 provides a block diagram of the instrument. The LOWL is weatherproof and requires no external dome or housing. It sits on two concrete piers and is inclined at an angle equal to the local latitude. The instrument is divided into an optics bay above, and an electronics bay below. A heliostat feeds light into the optics bay which contains the imaging optics, the auto-guider, the Doppler analyzer and detector. The electronics bay contains the camera electronics, stepper motor and temperature controllers, power supplies, and lightning protection. Instrument control and data acquisition functions are handled by a computer located in the adjacent observatory building. Watertight conduit carries power and signal cables between the computer rack and the instrument. All of the instrument subsystems are described in detail below. A summary of the instrument specifications is given in Table I.

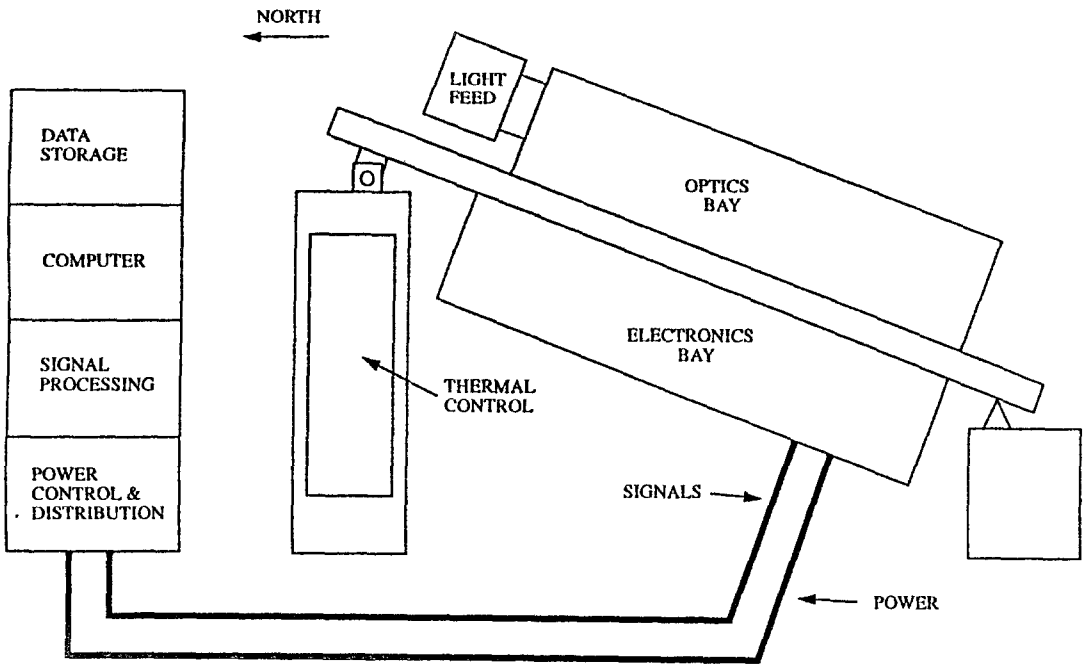

Fig. 1. Block diagram of the LOWL. The instrument sub-systems are shown to the right and the data acquisition and instrument control sub-systems are shown to the left.

TABLE I

LOWL instrument specifications

Observation type	Velocity imaging
Doppler analyzer	Magneto-optical filter
Absorption line	Potassium, 769.9 nm
Spatial resolution	25 arc sec
Field-of-view	Full disk
Sampling rate	15 s per velocity image
Random noise	15 m s^{-1} per pixel
Zero-point noise	6 cm s^{-1} r.m.s.

3.1. OPTICAL SYSTEM

The optical components of the LOWL are shown schematically in Figure 2. A heliostat light feed, which represents the only moving part of the entire instrument, is used to track the Sun and direct the solar beam along the optical axis. It has an Al coated elliptical flat mirror with minor and major axes of 66 mm by 93 mm. The light feed is driven by two stepper motors coupled to absolute encoders which

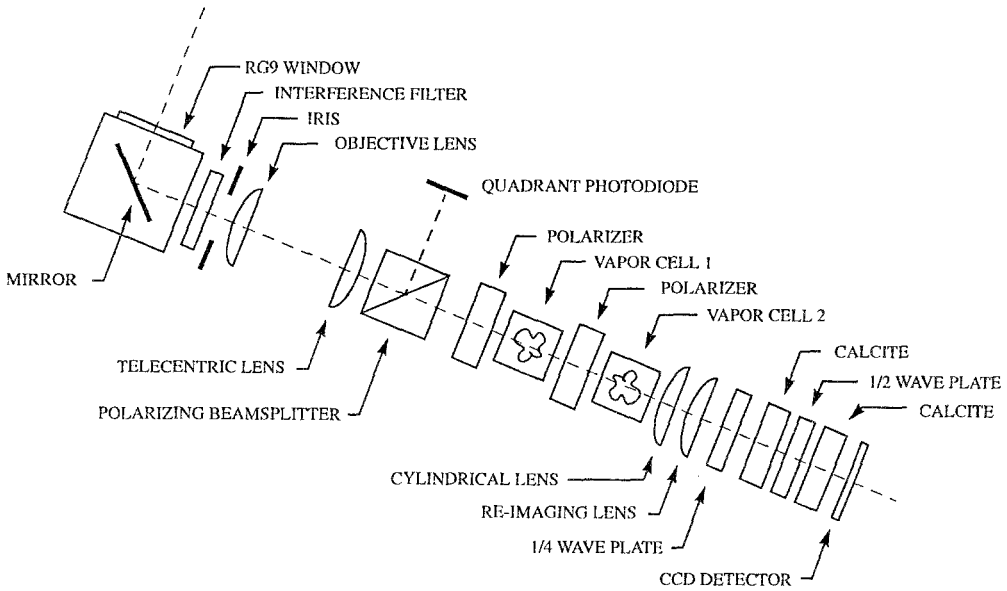

Fig. 2. Schematic diagram of the LOWL optical components. The diagram is not to scale.

provide daily tracking of the solar hour angle (HA), and declination (DEC) motion. The HA motor has its output reduced by a harmonic drive speed reducer of 200:1 ratio, while the DEC motor drives a worm and sector gear having 360:1 reduction. The motors are microsteppers with a step size of 1.3 arc sec in HA and 1.4 arc sec in DEC after reduction. The HA motor is driven at a constant rate throughout the day, and the position of both motors is updated every 15 seconds according to position information obtained by the auto-guider. Errors in the harmonic drive reducer limit the pointing accuracy of the light feed to $\sim$ 8 arc sec r.m.s., which is small in comparison to the spatial resolution of 25 arc sec. The heliostat box is weatherproof and sealed with an entrance window of 3 mm thick Schott RG-9 which has been wedged at an angle of 30 arcmin to suppress fringes. The RG-9 has a transmission of 86% at 770 nm, $< 1\%$ for wavelengths below 700 nm and an average transmission of $< 6\%$ between 1.2 and 5 μ. By modeling the variation of heliostat pointing errors throughout the day, we have iteratively aligned the rotation axis of the heliostat to the Earth's polar axis to within $\sim 0.1°$. The heliostat causes the solar image to rotate uniformly on the detector at a rate of 360° per day. This effect is removed as a part of the data analysis.

Immediately following the light feed are the interference filter, iris and objective lens. The interference filter has a maximum transmission of 50% at 770 nm, and full-width at half-maximum of 2.9 nm. The objective lens is simple plano-convex with a focal length of 600 mm, stopped down to an aperture of 9 mm by the iris. The diffraction limit of this aperture is $\approx$ 22 arc sec at 770 nm and roughly corresponds to the resolution allowed by the CCD detector. A plano-convex telecentric lens, focal length 250 mm, is located one focal length behind the solar image formed

by the objective lens. This lens collimates the solar image and forms an image of the objective near the second atomic vapor cell. Following the telecentric lens, a portion of the beam is diverted into an auto-guider (see Section 3.2). The undiverted beam passes through the Doppler analyzer where light in opposite wings of the solar absorption line is encoded into circular polarization state (see Section 3.3). A re-imaging lens then focuses the beam through the separator, which displaces the two filtered images, and onto the CCD detector. The beam separator is described in Section 3.3.2. The re-imaging lens is composed of a plano-convex lens and a meniscus lens separated by 0.87 mm forming 1.5 mm diameter solar images on the detector. All lenses are BK7 and have been coated with anti-reflection coatings which have $< 0.2\%$ reflection per surface at 770 nm. Ray tracing of the optical system indicates an r.m.s. spot size less than 2 microns (2.5 arc sec) over the $\sim 0.25^\circ$ solar field of view. This smearing is small in comparison to the pixel size.

3.2. AUTO-GUIDER

An auto-guider has been incorporated into the optical system to facilitate image acquisition and remove the tracking errors of the heliostat. It consists of a polarizing beamsplitter which diverts half of the incoming light vertically through a 150 mm focal length lens which forms a 2.2 mm diameter solar image on a quadrant photodiode. The beamsplitter cube measures 50 mm on a side and has $< \lambda/10$ transmitted wavefront distortion across its aperture. The 10 mm diameter of the photodiode limits the auto-guider field of view to $\pm 1.1^\circ$. The polarization state diverted by the beamsplitter is later absorbed by a linear polarizer, so this unit does not reduce the light available to the remainder of the instrument. The outputs of the photodiode go directly into electronics which form sum and difference signals of opposite quadrants. These signals are then digitized at the computer and used to update the position of the light feed. Noise from the photodiode at normal light levels allows the position of the solar image to be determined to better than 1 arc sec.

3.3. DOPPLER ANALYZER

3.3.1. *Magneto-Optical Filter*

The Doppler analyzer for this instrument is based on a magneto-optical filter (MOF), which employs atomic vapors of potassium in longitudinal magnetic fields to create two very narrow bandpass filters in the wings of the solar absorption line at 769.9 nm. The theory of MOFs and their application in the solar context has been discussed by Cimino, Cacciani, and Fofi (1968), Cimino, Cacciani, and Sopranzi (1969), Agnelli, Cacciani, and Fofi (1975), Cacciani and Fofi (1978), Cacciani *et al.* (1991), Lin and Kuhn (1989), and others.

The configuration of the MOF Doppler analyzer is shown schematically in Figure 3. The input light initially passes through a linear polarizer and into the

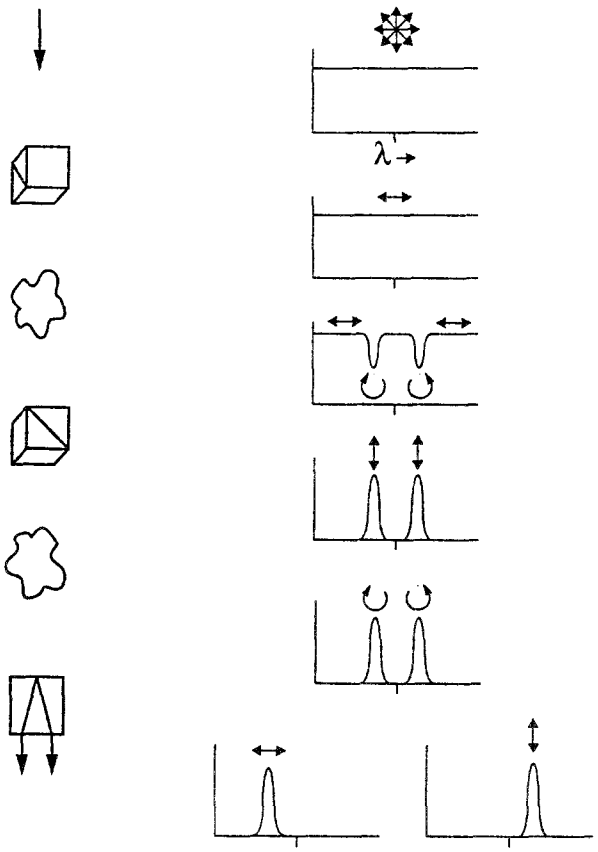

Fig. 3. Schematic of the MOF operating principles. Optical components are shown to the left, while the evolution of the transmission profile is shown to the right. Polarization states are indicated by the arrows above the transmission profiles.

first atomic vapor in a 3 kG longitudinal magnetic field. The inverse Zeeman effect (circular dichroism) of the vapor converts the linear light to circularly polarized light by removing the complementary circular polarization in the vicinity of the sigma components. Half of this circularly polarized light is transmitted through the second linear polarizer which has its transmission axis perpendicular to the first. Any light with polarization state not modified by the vapor, such as continuum, will be extinguished by the second crossed polarizer. This results in narrow transmission peaks on both sides of line center at the positions of the sigma components. In general, the Faraday effect (circular birefringence) of the vapor can rotate the plane of input linear polarization and also cause transmission through the crossed polarizers. However, the optical depth of this potassium vapor is kept low enough that this effect is not important.

The inverse Zeeman effect of a second vapor in an identical longitudinal magnetic field will convert the linearly polarized light into opposite circularly polarized

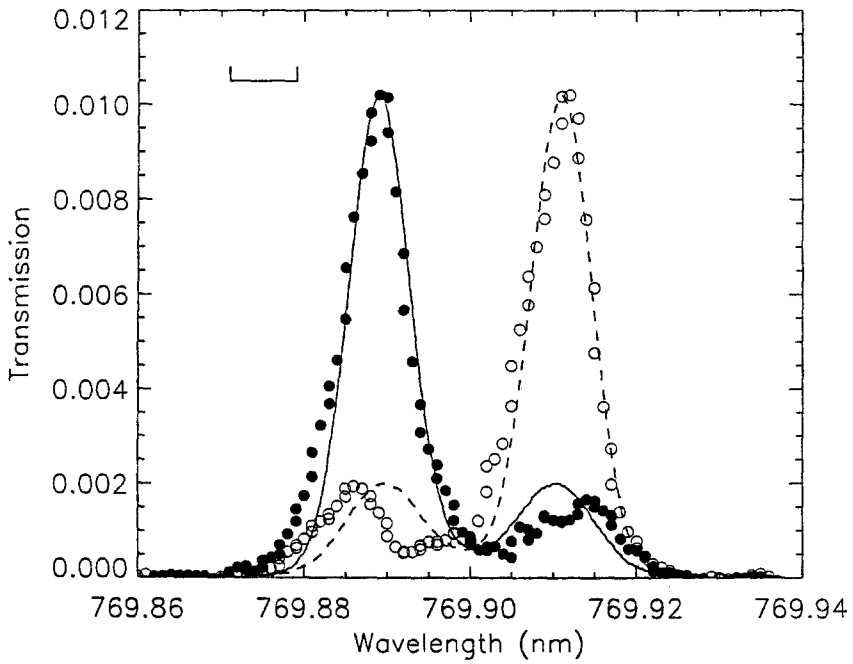

Fig. 4. Measured (open and filled circles) and theoretical (solid and dashed lines) transmission profiles for the MOF used in the instrument. The horizontal line in the upper left indicates the spectrograph resolution.

light in opposite wings of the line. This encodes wavelength information into circular polarization state. The beams are optically separated by converting circular polarizations into orthogonal linear polarizations with a quarter-wave plate, and displaced by a modified Savart plate. The images in the two wavelength bands are then focused onto a single CCD detector.

Figure 4 shows a spectrograph measurement of the MOF transmission profiles. The solid and dashed lines in the figure are theoretical profiles generated with a simple model of the MOF in the large field approximation (Tomczyk, 1988). The theory has been smeared with a gaussian to simulate the effect of the spectrograph resolution. The transmission scale is from the theory and does not account for losses in the MOF due to reflections at air-glass interfaces and the transmission of the pre-filter. The agreement between the measurements and the theory is good, however, the widths of the measured profiles are dominated by the spectrograph contribution. The actual MOF profiles are more closely given by the unsmeared theoretical profiles which are shown in Figure 5(a). The MOF instrument profiles have a maximum transmission of $\sim$ 4% and a bandwidth of $\sim$ 2 pm.

Also on Figure 5(a) is plotted the solar absorption line profile for the potassium line at 769.9 nm measured by the Kitt Peak FTS at disk center. The depth and width of this line make it ideally suited for solar velocity measurements, with a line depth

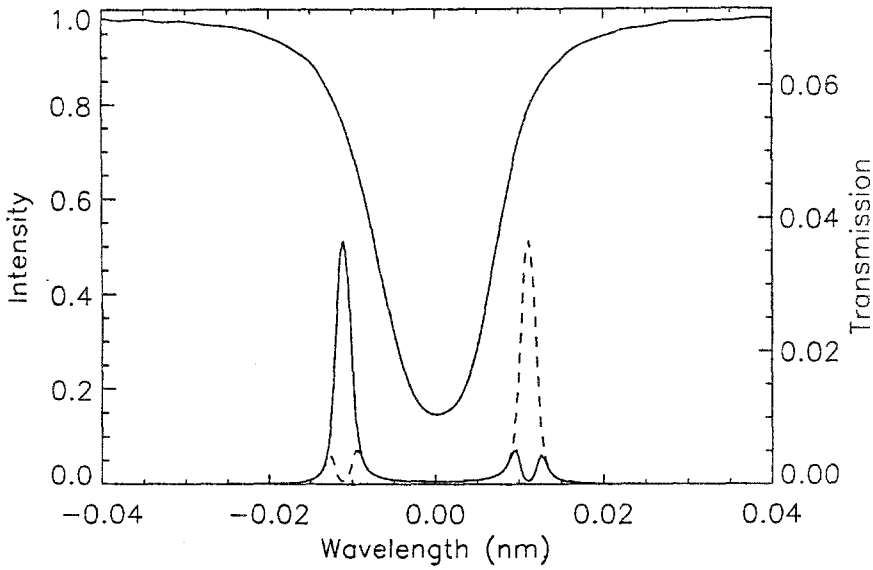

Fig. 5a.

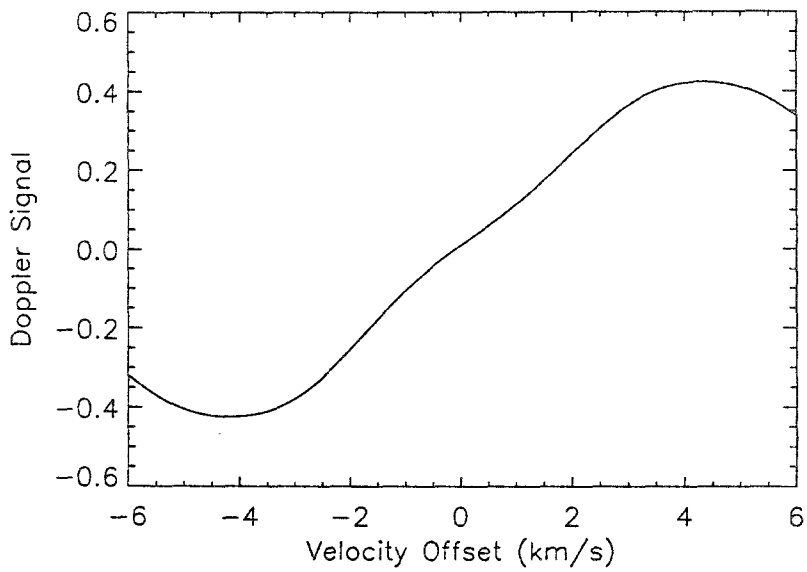

Fig. 5b.

Fig. 5a–b. The unsmeared theoretical MOF profiles are shown in (a), along with the solar absorption line profile. The resulting Doppler response of these profiles is shown in (b).

of 85% of the continuum and full-width at half-maximum of 16 pm (6.2 km s^{-1}, Snider, 1972). In addition, the line is highly symmetric and is free from solar or telluric blends. The potassium line is formed in the solar atmosphere at an altitude

just below the temperature minimum (De la Reza and Müller, 1975), and displays little limb shift (Andersen *et al.*, 1985).

From the measured intensities in the wings of the line, we compute the ratio of the difference of the intensities to the sum. We call this ratio the Doppler signal, and assume it is linearly related to the radial velocity as

$$v = k\frac{I_b - I_r}{I_b + I_r} + v_0 \,, \tag{1}$$

where v is the radial velocity, k is the calibration constant which has the same units as v, I_b and I_r are the intensities through the blue and red bandpasses, and v_0 is the systematic velocity. The profiles of Figure 5(a) were used to compute the velocity response of the MOF, and the resulting variation of the Doppler signal as a function of solar velocity offset is shown in Figure 5(b). The plot shows that this MOF has a reasonably linear response over a range of about ± 3.5 km s^{-1}. The magnitude of this range is set by the separation of the two MOF bandpasses; the magnetic fields of the MOF were chosen to provide the maximum allowable separation.

The calibration constant k can be determined empirically by two different methods. One method uses the observed variation of radial velocity across the solar disk introduced by solar rotation, and the other uses the variation in the systematic velocity due to Earth rotation and orbit. The solar rotation method is preferable since it allows calibration over a much larger velocity range (4 km s^{-1}) than the ephemeris method (≈ 0.8 km s^{-1}). We find that typically $k \approx 8500$ m s^{-1}. In practice, the instrument is calibrated daily with the rotation method, and the ephemeris method is used as a consistency check.

The Doppler analyzer used here has several desirable characteristics. The atomic vapors make the wavelength zero-point extremely stable (see Section 4 for further discussion). The simultaneous measurement of the intensity through the two transmission bands eliminates noise sources due to atmospheric and instrumental image motion, and intensity variations caused by atmospheric transmission, exposure time variation, etc. Also, this design results in a Doppler analyzer with no moving parts, which is important in that it enhances the dependability of the instrument. It is interesting to note that the two-beam Doppler imaging technique was first employed by Leighton, Noyes, and Simon (1962) and led to their discovery of the solar oscillations.

3.3.2. *Beam Separator*

The modified Savart plate (Francon, 1957; Semel, 1987) used for beam separation is composed of two calcite rhombs of 15 mm thickness separated by a half-wave plate (refer to Figure 2). The thickness of the rhombs was chosen to provide an image separation of 3.2 mm on the CCD detector. The rhombs are cut in the natural cleavage planes, with the optic axis inclined at about 45° to the entrance face. The second rhomb is rotated 180° with respect to the first. A half-wave plate swaps ordinary and extraordinary rays midway through the beam separator and causes

the two images to have identical optical properties. The beam separator introduces a significant amount of astigmatism which is corrected by a cylindrical lens of 4400 mm focal length located in front of the beam separator. The two beams are not physically separated until immediately before the CCD detector in order to minimize any optical differences between the two images. The only optical element encountered by the two beams after separation is the protective window of the CCD detector. If the half-wave plate is not exactly half-wave, a small fraction of the beam will pass undeviated through the beam separator and form a ghost image midway between the split images. A beam separation of 3.2 mm and image size of 1.5 mm were chosen so that the two images would not overlap with the ghost image.

3.3.3. *Magnetic Field Geometry*

The configuration of the atomic vapor cells and magnets are identical for the two vapor cells. Four neodymium-iron-boron magnets are placed on each of two pure iron pole pieces to form a longitudinal magnetic field of 3 kG at the center of a vapor cell. Steel bars are used to connect the field and for structural integrity. Over the central 2 cm of the cell the axial field strength is uniform to ± 0.2 kG, and the transverse field is < 0.1 kG. The strength of the longitudinal field was tuned by placing steel spacers between the magnets and the pole pieces. We have seen no degradation of the field strength after many assembly/dis-assemblies of the magnet units and many thermal cycles of the vapor cells. The magnet vendor quotes a magnet strength degradation of 1% per century when the magnets are maintained at temperatures below 60 °C.

3.3.4. *Non-Ideal MOF Properties*

The MOF implemented here has several non-ideal properties which warrant further discussion. One property is that the continuum is extinguished to a level set by the extinction ratio of the polarizers. The Glan–Thompson calcite polarizers employed here have an extinction ratio of a few$\times 10^{-6}$. Even so, the ratio of the MOF bandpass to the wavelength range of detector sensitivity is comparable to the polarizer extinction ratio. The 2.9 nm interference filter was included in the optical system to reduce this continuum contribution to a negligible level.

We have found that a small amount of birefringence is present in the exit window of the second vapor cell. This is important because the beams are encoded by polarization state at this point, and birefringence can redistribute the signal of the beams. We find that this redistribution is small, about 2%, and is one source of an instrumental bias velocity. Similarly, stress in the windows of the first vapor cell can also introduce linear birefringence which can modify the polarization state of the continuum and allow its partial transmission through the crossed polarizers. The birefringence in the cell windows has been minimized by carefully mounting the windows without stress, and maintaining the windows at a uniform temperature.

The heliostat mirror is an elliptical polarizer whose plane of polarization rotates throughout the day with the degree of polarization depending weakly on the solar declination. This causes a modulation of the intensity through the instrument of a few percent throughout the day. To minimize this effect, we have oriented the Doppler analyzer so that minimum transmission occurs at 0 hour angle where the atmospheric extinction is a minimum.

The potassium used for this study includes the naturally occurring isotope K^{41}. The abundance ratio of K^{39} to K^{41} is 13.5 : 1 and the isotope shift is 176 m s^{-1} (Jackson and Kuhn, 1938). The effects of the K^{41} isotope were included in the MOF model, and simulations indicate that under typical operating conditions transmission due to the K^{41} is about 2% of that due to the K^{39}. This K^{41} transmission introduces a bias velocity of a few m s^{-1}. The simulations also show that the presence of K^{41} does not significantly degrade the temperature stability of the instrument.

Another source of an instrumental bias velocity is the pressure shift introduced by the 35 mmHg of Ar buffer gas in the vapor cells. Using the data of Allard and Keilkopf (1982), we have estimated that the buffer gas produces a red shift of our transmission bands of about 250 m s^{-1}. We are currently investigating the possibility of using this pressure shift to compensate for the solar gravitational redshift. All of the sources of instrumental bias velocity appear to be uniform over the field of view, and stable over timescales of interest.

3.4. DETECTOR/FRAME GRABBER

The detector for the instrument is a COHU Series 6500 CCD camera based on a Tektronix TC-245 chip. It has a quantum efficiency of 0.45 at 770 nm and a format of 739 columns by 434 rows, although only the first 128 rows are used. The pixels are rectangular and measure 8.5 $\times$ 19.75 μ which corresponds to 11 by 25 arc sec on the Sun. Since the solar image rotates on the detector, the vertical size of the pixels effectively limits the spatial resolution of the instrument to 25 arc sec.

The CCD camera is read out at a rate of 6 Hz, and the images are digitized to 8-bits and accumulated in a 32-bit frame buffer. Digitization is synchronized to the pixel clock of the CCD. Random noise in darkness has been measured at 1.2 ADU readout^{-1} pixel^{-1} (360 e^-), and at the typical light level at disk center (0.75 saturation) is 2.7 ADU readout^{-1} pixel^{-1}. The camera/frame grabber combination is far from photon noise limited, however, averaging 48 images per observation at this noise level results in a signal-to-noise ratio in excess of 500:1.

The differential nonlinearity of the the A/D converter in the frame grabber board has been accurately measured and amounts to 0.17 LSB r.m.s. This allows the signal-to-noise ratio of the averaged images to exceed the 8-bit quantization of the A/D converter.

3.5. INSTRUMENT CONTROL AND DATA ACQUISITION

In order to maximize the duty cycle of the observations and minimize the demands on our small observatory staff, the instrument has been highly automated. For simplicity, we have adopted a Press On Regardless mode of operation where no decisions are made by the instrument or observers about the quality of the observing conditions. The observing algorithm simply observes the Sun if it is above the horizon. The quad cell signals are used to point the light feed if the measured light level is above about 10% of the nominal light level, otherwise the light feed is pointed to the solar position as predicted by an ephemeris calculation. The burden of data quality assurance is placed on those performing data analysis.

While the Sun is above the horizon, the control system loops through the following sequence of actions: (1) The system waits for a 15-s boundary in Universal Time. (2) Forty-eight images are read from the CCD camera and accumulated into the frame buffer. (3) Camera data and housekeeping information including voltages, temperatures, and guiding information are collected and written to tape. (4) The light feed pointing is updated according to the auto-guider signals after filtering through a digital servo.

All instrument control and data acquisition functions are performed by a 386/33-based industrial grade PC computer. Control of the heliostat motors and temperature controllers is accomplished through high level commands sent by the PC via serial communication ports. Voltages from the temperature sensors and auto-guider pass through a custom signal conditioning board and are digitized to 12 bits by a board in the PC. The time base for the experiment is maintained by a WWVH receiver board plugged into the PC. The system includes a pair of 8-mm digital tape drives which are interfaced to the PC through a SCSI bus adapter. Each of the drives are capable of storing three to four days of observations. A real-time display shows the raw filtergram images, a computed Doppler image, instrument temperatures, and solar ephemeris quantities. This color coded information is sufficient to allow the observer to periodically verify proper instrument operation. Though an observer is on site nearly every day, the instrument can operate unattended for approximately one week.

Every hour a bias image is obtained by pointing the light feed 10° away from the Sun. Also at this time, a series of images are taken with the solar position offset 0.05° in 8 directions. These are used to compute a gain table using the method of Kuhn, Lin, and Loranz (1991).

3.6. THERMAL CONTROL

Thermal control of the atomic vapors is critical to maintain the stability of the velocity zero point. To accomplish this task, we employ two layers of thermal control. The first layer consists of a PID type temperature controller for each of the two potassium vapor cells. Each vapor cell has two potassium filled glass reservoirs

protruding horizontally from the glass body cell. Platinum resistive temperature sensors are bonded with thermally conducting epoxy to the outside of the potassium reservoirs in proximity to the evaporating metal surface. The glass reservoirs and central part of the cell are covered with a layer of copper mesh for heat distribution. Heating is provided by winding the reservoir with 5.5 ohm of 30 gauge nichrome wire. Finally, the reservoir exteriors are insulated by a layer of ceramic putty. We find that the copper is particularly critical in removing temperature gradients around the reservoirs.

The second thermal control layer maintains the air flowing through the instrument at a constant temperature of 32 °C. This is accomplished by forcing air through a servo-controlled heater, through the instrument, and then through a heat exchanger. The heat exchanger conducts heat across a central partition in an environmentally sealed box where the heat is removed by external air while maintaining the instrument air in a closed loop. A variable speed fan regulates the flow of external air through the heat exchanger box.

Solid state sensors monitor the temperature at various points within the instrument including the light feed and motors, the optics and electronics bays, as well as the external air temperature. Also, thermocouples are placed adjacent to the MOF reservoir sensors to provide an independent monitor of the reservoir temperatures. All of the sensors are interrogated every 15 s and logged with the data.

Careful attention has been paid to thermal loads in the system. Solar heating of the light feed interior is kept to a minimum by the RG-9 entrance window. All exterior walls have been insulated with a 22 mm layer of poly-isocyanate foam board, and the exterior of the instrument has been painted with high emissivity white paint.

4. Instrument Evaluation

The MOF is subject to several sources of noise. The relative contributions of instrumental noise sources can be estimated by considering the relationship between measured intensities and radial velocity given by Equation (1) in Section 3.3.1. Application of the propagation of errors to Equation (1) assuming the errors in the various quantities are uncorrelated and v_0 is small with respect to v gives

$$\left(\frac{\delta v}{v}\right)^2 = \left(\frac{\delta(I_b - I_r)}{I_b - I_r}\right)^2 + \left(\frac{\delta(I_b + I_r)}{I_b + I_r}\right)^2 + \left(\frac{\delta k}{k}\right)^2 + \left(\frac{\delta v_0}{v}\right)^2, \qquad (2)$$

where the δ's are the errors in the variables.

4.1. Random Noise Sources

We evaluate the random noise sources first and consider only the first two terms on the right-hand side of Equation (2). Using $\delta(I_b - I_r)^2 = \delta(I_b + I_r)^2 = \delta I_b^2 + \delta I_r^2$ and assuming $\delta I_b \approx \delta I_r = \delta I$, we find

$$\delta v \approx \frac{k}{\sqrt{2}} \frac{\delta I}{I} . \tag{3}$$

If the noise from each pixel can be assumed uncorrelated and there are 10^4 pixels, the solar noise contribution of 0.5 m s^{-1} translates into a requirement of 50 m s^{-1} per pixel r.m.s. Assuming a value of k of 8500 m s^{-1}, a random $\delta v = 50$ m s^{-1} will be reached for $I/\delta I = 120$. This represents the minimum random signal-to-noise ratio requirement per pixel. Also, this sets the minimum accuracy to which bias and gain correction must be performed. This requirement is not difficult to satisfy. In practice, a signal-to-noise ratio of 500 : 1 is achieved per observation which corresponds to a random noise of 15 m s^{-1} pixel^{-1} per observation.

4.2. SYSTEMATIC NOISE SOURCES

Systematic velocity errors will cause a variation in the mean solar velocity which will directly compromise the measurement of the $l = 0$ mode, and indirectly other low-degree modes via the mode leakage discussed in Section 2. In this instrument, systematic errors are caused by the variation of k and v_0 in response to changes in the optical depth of the potassium vapors induced by reservoir temperature variations. We can estimate the systematic errors by considering the last two terms in Equation (2):

$$\left(\frac{\delta v}{v}\right)^2 = \left(\frac{\delta k}{k}\right)^2 + \left(\frac{\delta v_0}{v}\right)^2 . \tag{4}$$

The velocity at a point on the disk can vary by either a change in the systematic velocity, or a change in the instrument sensitivity which changes the gradient of the velocity across the disk. The gradient has its greatest effect at the east and west limbs. After substituting for the velocity, assuming v_0 is small, and assuming that the variations in δk and δv_0 are due to temperature changes, we can write

$$\delta v^2 = \left(\frac{I_b - I_r}{I_b + I_r}\right)^2 \left(\frac{\partial k}{\partial T}\right)^2 \delta T^2 + \left(\frac{\partial v_0}{\partial T}\right)^2 \delta T^2 . \tag{5}$$

The variation of v_0 and k has been measured as a function of the temperature of the first and second vapor cell reservoirs (hereafter called vapor 1 and vapor 2), and is shown in Figure 6. Parabolic fits to the loci of points at constant vapor 1 temperature are superimposed on the data. The temperature coefficients for v_0 have been derived directly from the fits, while the temperature coefficients for k combine the fits with the assumption of a Doppler signal of 0.1 which occurs midway between disk center and the limb along the equator. We find

$$0.1 \frac{\partial k}{\partial T_1} = -14 \,\mathrm{m\,s^{-1}\,C^{-1}} , \qquad \frac{\partial v_0}{\partial T_1} = 2 \,\mathrm{m\,s^{-1}\,C^{-1}} ,$$

$$0.1\frac{\partial k}{\partial T_2} = -24\,\mathrm{m\,s^{-1}\,C^{-1}}\,, \qquad \frac{\partial v_0}{\partial T_2} = 0.4\,\mathrm{m\,s^{-1}\,C^{-1}}\,,$$

where the 1 and 2 subscripts refer to vapors 1 and 2. These results show that the systematic error in the velocity is more sensitive to changes in k than to changes in v_0. The variation of k is primarily due to incomplete absorption of the opposite transmission band by the second vapor. The small variation of v_0 is due to the symmetrical variation of the MOF profiles around the central wavelength and the stability of the central wavelength provided by the atomic vapor. The k sensitivity is not a function of the mean solar velocity, however, the v_0 coefficients increase with velocity but remain at the m s^{-1} C^{-1} level.

These measurements indicate that the reservoirs must be stabilized to a level of about 0.02 C to reach the 0.5 m s^{-1} level. To evaluate the LOWL temperature stability, we have taken typical measurements of the temperature fluctuations of the MOF reservoirs and converted them to velocity fluctuations using the above sensitivities. Figure 7 is a plot of the power spectra of these induced velocity fluctuations, compared with an estimate of the solar background spectrum (Harvey, 1985). The figure shows that the induced velocity noise is well below the solar noise background over the 5-min band and approaches the solar noise at $\sim$ 10 mHz. Integration of the instrument noise spectrum between 1 and 10 mHz amounts to 6 cm s^{-1} r.m.s. This indicates that the LOWL temperature control is sufficient to allow solar noise limited observations.

5. Preliminary Observations

The LOWL instrument began making routine observations in Hawaii on 26 February, 1994. A detailed description of the data and analysis procedures will be given elsewhere. Here we present only some results which bear on instrument performance.

Figure 8 shows the variation of radial velocity across the solar equator after calibration assuming a linear relationship between Doppler signal and velocity. These data are from the average of Doppler images taken over one hour around midday on 8 March, 1994. Neglecting limb shift, the projection of the solar rotation produces a linearly varying velocity across the solar disk with an amplitude of ± 2 km s^{-1}. At this time of year the Earth–Sun velocity was near maximum, and the west limb of the Sun had a recessional velocity near 3 km s^{-1}. The solid line is a straight line fit to the data for fractional radii between $\sim$ 0.9. The figure verifies that the observed Doppler signal is a linear function of the radial velocity over a range of at least ± 3 km s^{-1}.

The bottom curve of Figure 9 shows the variation of the systematic velocity with time over the course of one day. It was computed by taking the mean velocity over the solar disk for all of the images taken on 5 June, 1994. Superimposed on the plot is a curve showing the theoretical variation of radial velocity due

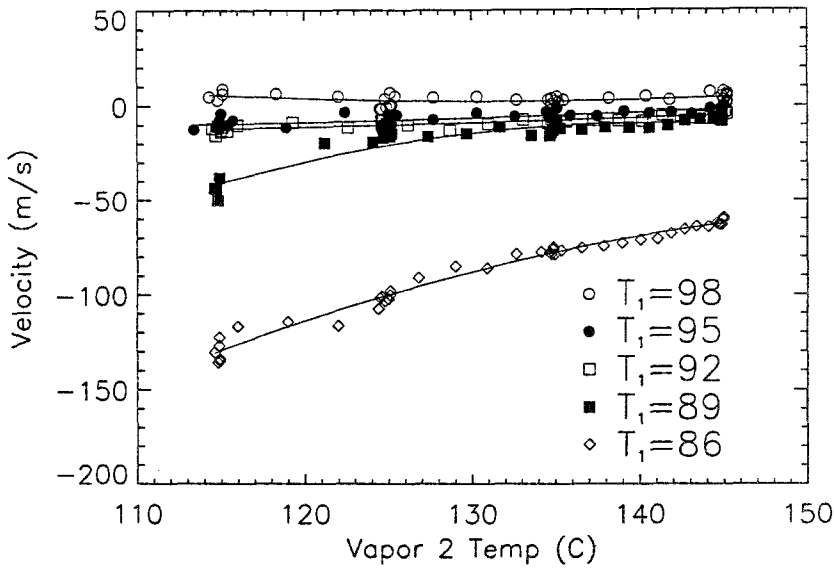

Fig. 6a.

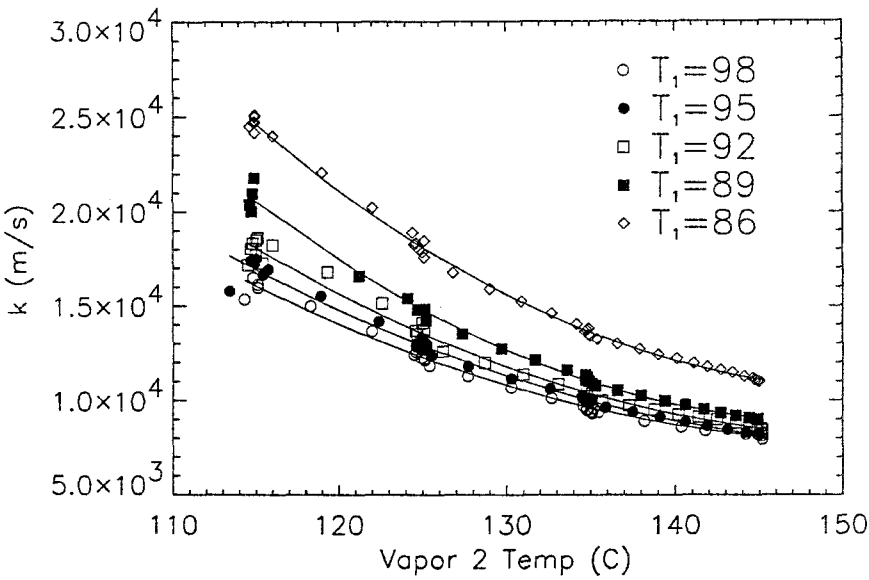

Fig. 6b.

Fig. 6a–b. Average velocity (a) and calibration constant k (b) are shown as a function of the temperatures of the two vapors. The solid lines are parabolic fits at constant vapor 1 temperature.

to the Earth's orbit and rotation, plus a constant offset of 636 m s^{-1} for solar gravitational redshift. That the observed systematic velocity closely tracks the theoretical variation attests to the stability of the instrument over time scales of a day. The offset between the observed and theoretical velocities is due to the

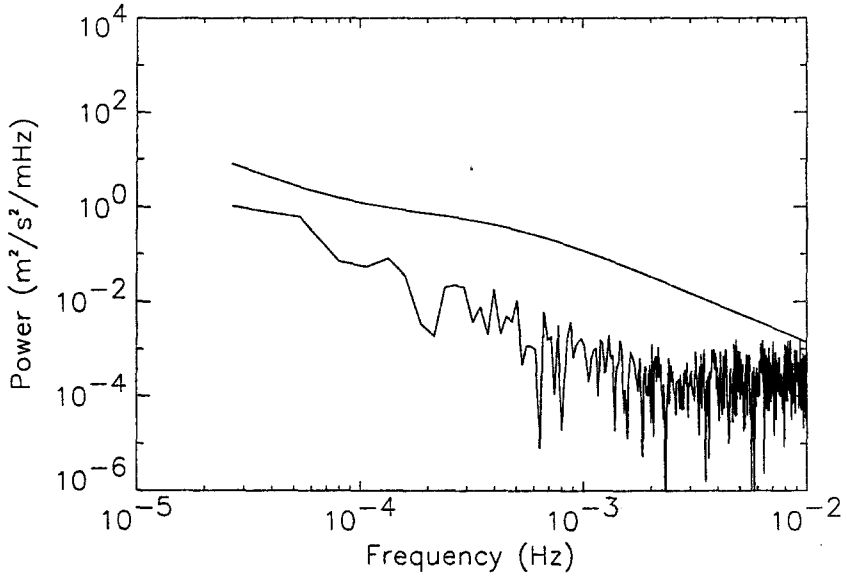

Fig. 7. Spectrum of velocity noise induced by vapor temperature fluctuations. The solid line is an estimate of the solar background velocity noise spectrum.

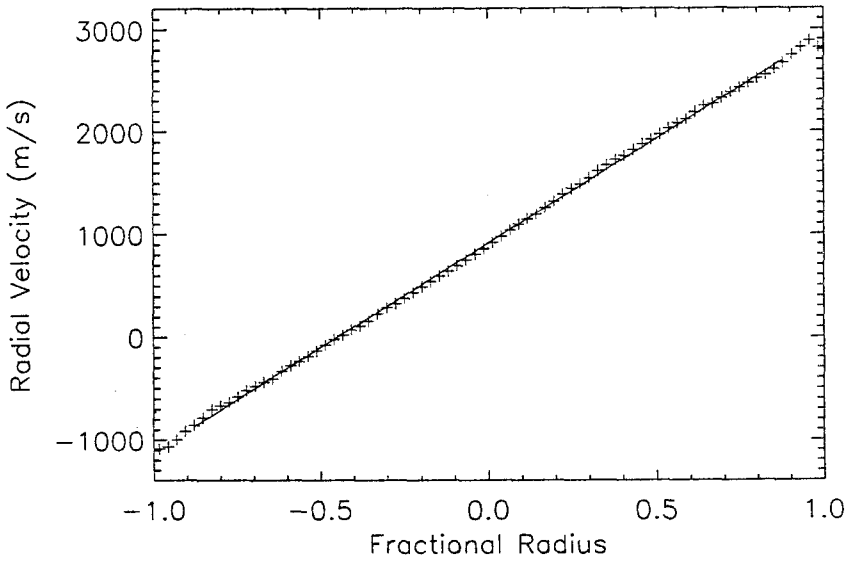

Fig. 8. Observed variation of the radial velocity across the solar equator. The solid line is a linear fit to the data between fractional radii of ±0.9.

instrumental bias velocity (see Section 3.3.4). This offset is stable with time and is corrected by simply subtracting a constant from the observed velocities.

Figure 10 shows the $l = 0$ power spectrum resulting from the analysis of the first 3 months of data. Solar oscillations are clearly visible with high signal-to-noise,

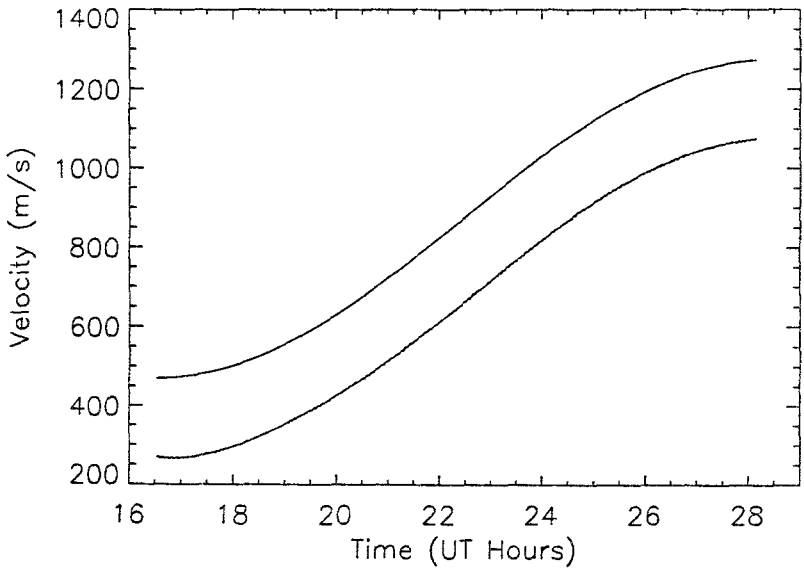

Fig. 9. Plot of the average velocity (lower curve) and the ephemeris velocity throughout the day of 5 June, 1994.

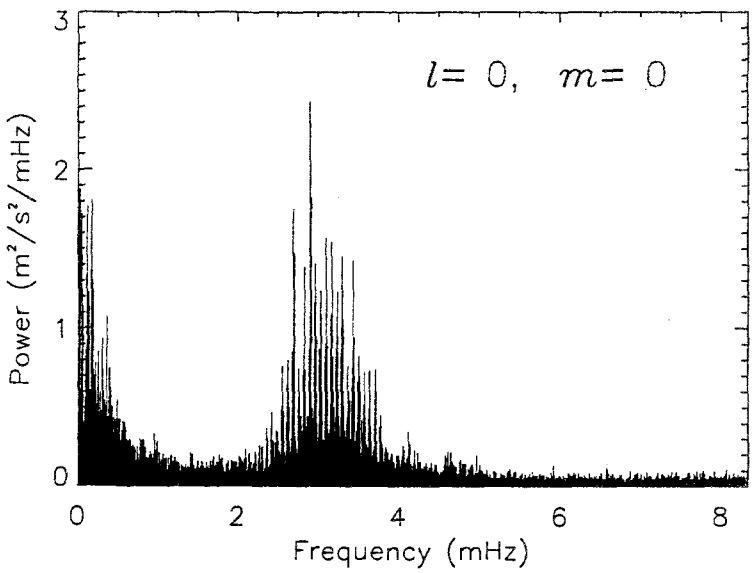

Fig. 10. Spectrum for degree $l = 0$ from the first 3 months of data.

and the rise in power at low frequencies is approximately consistent with the solar background noise spectrum. This verifies that the LOWL instrument is sufficiently stable to allow observations of the low-degree solar oscillations.

6. Summary

The LOWL instrument is uniquely qualified for the observation of low-degree oscillations. The combination of a potassium magneto-optical filter with a two-beam detection technique results in an instrument extremely stable against zero-point drift and immune to noise sources due to intensity fluctuations and image motion. The Doppler analyzer is linear over a wide velocity range and has no moving parts. The CCD camera and frame grabber combination allows the measurement of velocities accurate to 15 m s^{-1} per 15-s observation at a spatial resolution of 25 arc sec. Also, careful design of the thermal control system has resulted in instrumental noise of 6 cm s^{-1}s integrated over the 5-min band, which is almost an order of magnitude below the solar noise level. Instrument performance has been confirmed by the preliminary analysis of initial data.

We expect that one year of LOWL observations will be sufficient to constrain the rotation rate at $0.1 \pm 0.05\ R_\odot$ to within about 20%. This measurement will have important implications in many areas of solar and stellar physics.

Acknowledgements

We would like to acknowledge the assistance provided by Seth Veitzer, Bifford Williams, Clarke Chambellan, Terry Leach, and Paula Rubin during the development and construction of the instrument. We thank Peter Nelson for helpful advice on the thermal design. S.T. gratefully acknowledges the critical support provided by Jeffrey Schuenke early in the project, and thanks M. J. Thompson for discussions motivating this research. We would like to thank Greg Ladd for communicating the NSO/Kitt Peak FTS data which were produced by NSF/NOAO, and Mike Scherer of Kelty Pack Inc. for use of a sunshade and hammer drill for the installation. We acknowledge the support provided by Eric Yasukawa and Daryl Koon of MLSO during the deployment of the instrument and for the continued collection of the observations. We thank O. R. White, T. Brown, T. Apporchaux, and J. Kuhn for comments on the manuscript. A.C. acknowledges support from the University of Rome. This work was supported by the NSF through base funding of HAO/NCAR.

References

Agnelli, G., Cacciani, A., and Fofi, M.: 1975, *Solar Phys.* **44**, 509.

Allard, N. and Keilkopf, J.: 1982, *Rev. Mod. Phys.* **54**, 1103.

Andersen, B. N., Barth, S., Hansteen, V., Leifsen, T., Lilje, P. B., and Vikanes, F.: 1985, *Solar Phys.* **99**, 17.

Brown, T. M., Mihalas, B. W., and Rhodes, E. J., Jr.: 1986, in J. Christensen-Dalsgaard and S. Fransden (eds.), *Physics of the Sun*, Vol. 1, D. Reidel Publ. Co., Dordrecht, Holland, p. 453.

Cacciani, A. and Fofi, M.: 1978, *Solar Phys.* **59**, 179.

Cacciani, A., Rosati, P., Ricci, D., Egidi, A., Apporchaux, T., Marquedant, R. M., and Smith, E. J.: 1991, *JPL Publication*, No. 11900, Pasadena, California.
Christensen-Dalsgaard, J., Gough, D. O., and Toomre, J.: 1985, *Science* **229**, 923.
Christensen-Dalsgaard, J., Gough, D. O., and Thompson, M. J.: 1991, *Astrophys. J.* **378**, 413.
Charbonneau, P. and MacGregor, K. B.: 1992, *Astrophys. J.* **387**, 639.
Cimino, M., Cacciani, A., and Fofi, M.: 1968, *Solar Phys.* **3**, 618.
Cimino, M., Cacciani, A., and Sopranzi, N.: 1969, *Appl. Optics* **7**, 1654.
Claverie, A., Isaak, G. R., McLeod, C. P., van der Raay, H. B., and Roca Cortes, T.: 1981, *Nature* **293**, 443.
Cox, A. N., Guzik, J. A., and Kidman, R. B.: 1989, *Astrophys. J.* **342**, 1187.
De la Reza, R. and Müller, E. A.: 1975, *Solar Phys.* **43**, 15.
Duvall, T. L. and Harvey, J. W.: 1986, in D. O. Gough (ed.), *Seismology of the Sun and the Distant Stars*, D. Reidel Publ. Co., Dordrecht, Holland, p. 105.
Duvall, T. L., Harvey, J. W., and Pomerantz, M.: 1988, in J. Christensen-Dalsgaard and S. Fransden (eds.), *Advanees in Helio- and Asteroseismology*, p. 37.
Dziembowski, W. A., Pamyatnykh, A. A., and Sienkiewicz, R.: 1991, *Monthly Notices Roy. Astron. Soc.* **249**, 602.
Francon, M.: 1957, *J. Opt. Soc. Am.* **47**, 528.
Gilman, P. A., Morrow, C. A., and DeLuca, E. E.: 1989, *Astrophys. J.* **338**, 528.
Goode, P. R., Dziembowski, W. A., Korzennik, S. G., and Rhodes, E. J., Jr.: 1991, *Astrophys. J.* **367**, 649.
Grec, G., Fossat, E., Brandt P., and Deubner, F. L.: 1977, *Astron. Astrophys.* **77**, 347.
Guzik, J. A. and Cox, A. N.: 1991, *Astrophys. J.* **381**, 333.
Guzik, J. A. and Cox, A. N.: 1992, *Astrophys. J.* **386**, 729.
Harvey, J. W.: 1985, in E. J. Rolfe and B. Battrick (eds.), *Future Missions in Solar, Heliospheric and Space Plasma Physics*, ESA Publications, Noordwijk, p. 199.
Harvey, J. W.: 1988, in E. J. Rolfe (ed.), *Seismology of the Sun and Sun-like Stars*, ESA Publications, Noordwijk, p. 55.
Hill, H. A., Bos, R. J., and Goode, P. R.: 1982, *Phys. Rev. Letters* **49**, 1794.
Jackson, D. A. and Kuhn, H.: 1938, *Proc. Roy. Soc. London* **A165**, 303.
Kuhn, J. R., Lin, H., and Loranz, D.: 1991, *Publ. Astron. Soc. Pacific* **103**, 1097.
Leighton, R. B., Noyes, R. W., and Simon, G. W.: 1962, *Astrophys. J.* **135**, 474.
Lin, H. and Kuhn, J. R.: 1989, *Solar Phys.* **122**, 365.
Loudagh, S., Provost, J., Berthomieu, G., Ehgamberdiev, S., Fossat, E., Gelly, B., Grec, G., Khalikov, S., Lazrek, M., Pallé, P., Régulo, C., Sanchez, L., and Schmider, F. X.: 1993, *Astron. Astrophys.* **275**, L25.
MacGregor, K. B. and Brenner, M.: 1991, *Astrophys. J.* **376**, 204.
Pinsonneault, M. H., Kawaler, S. D., Sofia, S., and Demarque, P.: 1989, *Astrophys. J.* **338**, 424.
Rhodes, E. J., Jr., Ulrich, R. K., and Simon, G. W.: 1977, *Astrophys. J.* **218**, 901.
Semel, M.: 1987, *Astron. Astrophys.* **178**, 257.
Snider, J. L.: 1972, *Phys. Rev. Letters* **28**, 853.
Sorenson, J. M.: 1988, in E. J.Rolfe (ed.), *Seismology of the Sun and Sun-like Stars*, ESA Publications, Noordwijk, p. 41.
Tomczyk, S.: 1988, Ph.D. Dissertation, University of California, Los Angeles.
Toutain, T. and Fröhlich, C.: 1992, *Astron. Astrophys.* **257**, 287.
Veitzer, S. A., Tomczyk, S., and Schou, J.: 1992, in T. M. Brown (ed.), *GONG 1992: Seismic Investigation of the Sun and Stars*, PASP Conference Series, Vol. 42, p. 465.
Vorontsov, S. V., Baturin, V. A., and Pamyatnykh, A. A.: 1991, *Nature* **349**, 49.
Wilson, P. R.: 1992, *Astrophys. J.* **399**, 294.